Synthetic normal faulting of the 9 January 2008 Nima (Tibet) earthquake from conventional and along-track SAR interferometry

Jianbao Sun,[1] Zhengkang Shen,[1] Xiwei Xu,[1] and Roland Bürgmann[2]

Received 18 August 2008; revised 29 October 2008; accepted 31 October 2008; published 29 November 2008.

[1] We use Synthetic Aperture Radar Interferometry (InSAR) to derive the coseismic deformation field of the 9 January 2008 Nima (Tibet) earthquake. The results show an asymmetric deformation pattern, consistent with normal faulting on a NW-dipping fault plane. The complex line-of-sight (LOS) fringe pattern suggests that a second, synthetic fault in the hanging wall of the mainshock rupture slipped during the event, most likely during the largest aftershock. We use conventional and along-track InSAR data to invert for the geometry and the slip-distribution on the two fault planes. The focal mechanisms of the mainshock and its largest aftershock show normal faulting with a small left-lateral strike-slip component near the NE-trending Riganpei Cuo fault, which is consistent with our InSAR observation and inversion result. This event suggests that normal faulting in addition to previously established conjugate strike-slip deformation in the region contributes to the internal deformation of central Tibet.
Citation: Sun, J., Z. Shen, X. Xu, and R. Bürgmann (2008), Synthetic normal faulting of the 9 January 2008 Nima (Tibet) earthquake from conventional and along-track SAR interferometry, *Geophys. Res. Lett.*, *35*, L22308, doi:10.1029/2008GL035691.

1. Introduction

[2] On 9 January, 2008, the Mw 6.4 Nima earthquake struck central Tibet, China. In the following two months, 37 aftershocks were recorded by the global seismic network. The largest (M_w 5.9) aftershock occurred on January 16, 2008. The USGS-CMT focal mechanisms of the mainshock and its largest aftershock show mainly normal faulting with dip angles of ~45°. The epicenter (32.235°N, 85.180°E) is near the boundary of Nima county (in the west) and Gaize county (Xizang, China). Because few people live in the remote region, there were no casualties reported in the earthquake.

[3] There continues to be much debate about the fundamental nature of deformation of the Tibetan plateau. While one school of thought envisions Tibet to be a thickened, weak and fluid-like zone [*England and Molnar*, 2005], others consider the tectonics in the region as that of essentially rigid microplates bounded by major lithospheric faults [*Peltzer and Tapponnier*, 1988]. Studies of Quaternary faults in central Tibet suggest that the eastward motion of Tibet may be accommodated by a large number of conjugate strike-slip faults distributed across central Tibet [*Taylor et al.*, 2003]. *Taylor et al.* [2003] investigated the conjugate faults along the Bangong-Nujiang suture zone and estimated a north–south contraction rate of ~1–2 mm/a and >2–4 mm/a of east–west extension across the 200–300 km wide central Tibet conjugate fault zone. *Zhang et al.* [2004] using 533 GPS points, inferred eastward stretching of 21.6 ± 2.5 mm/a between long 79°E and 93°E, which is roughly twice the N20°E convergence rate across the plateau interior of 10–14 mm/a.

[4] Central Tibet is an important region to study the accommodation of Indo-Asia collision across the Tibetan plateau. However, there have only been a few small historic earthquakes in the region of less than magnitude 5 to illuminate the active faulting style and distribution of deformation. The fault plane solutions of historical earthquakes show a combination of normal and strike-slip faulting with T-axes oriented approximately east–west [*Molnar and Lyon-Caen*, 1989]. The Nima earthquake happened near the southern termination of the left-lateral, NE-trending Riganpei Cuo fault at 85.2°E, where *Taylor and Peltzer* [2006] suggest a connection to the Bangong-Nujiang suture zone via small, west-dipping normal faults. *Taylor and Peltzer* [2006] measured the interseismic deformation across the Riganpei Cuo fault with InSAR and inferred a left-lateral strike-slip rate of ~3.4–11 mm/a. Here we examine the deformation associated with the 2008 Nima earthquake using InSAR LOS change and along-track measurements to improve our understanding of the geometry and slip of the largest historic event in the region in the context of its tectonic environment.

2. Data Processing Result of Conventional and Along-Track SAR Interferometry

[5] We rely on data from the ASAR sensor on the Envisat satellite of the European Space Agency, which has been in operation since 2002. The white rectangles in Figure 1 show the ground coverage of the data. Table 1 summarizes the data and their acquisition dates. Except the conventional InSAR processing, we also try to use the newer along-track SAR Interferometry technique to retrieve the azimuth deformation [*Barbot et al.*, 2008]. The data processing details can be found in the auxiliary materials.[1]

[6] We re-wrapped the final interferograms into 10 cm cycles after phase unwrapping and error corrections. Figure 2a shows the ascending interferogram. The LOS fringes are clear near the Nima-Gaize county boundary (the grey line) with maximum range increase of ~46.3 cm at the

[1]State Key Laboratory of Earthquake Dynamics, Institute of Geology, China Earthquake Administration, Beijing, China.
[2]Berkeley Seismological Laboratory, University of California, Berkeley, California, USA.

0094-8276/08/2008GL035691$05.00

[1]Auxiliary materials are available in the HTML. doi:10.1029/2008gl035691.

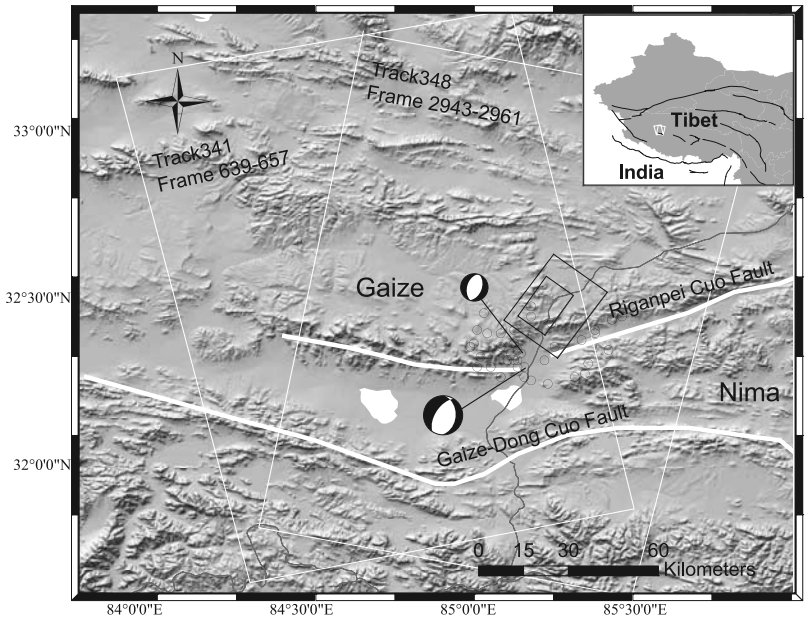

Figure 1. The location of the 9 January 2008 Nima earthquake in central Tibet. The topography is the 3 arc-second SRTM data. The two white boxes show the ground coverage of the Envisat SAR data in descending and ascending pass. The thick-white lines show the active faults in this region revised from *Deng et al.* [2002]. The empty-black circles show the mainshock and aftershocks of the Nima earthquake (USGS NEIC catalog). Note the offset between InSAR deformation and the teleseismic location. The thin-grey line shows the boundary between Nima county and Gaize county. The filled-white polygons denote small lakes. The two rectangles show the up-dip ground projection of the inferred fault planes used in the slip-distribution inversion (the fault top is near the east edge at 1.5 km depth). The insert map shows the India-Asia collision zone and the location of this earthquake.

center of the fringes. Toward the west of the dense concentric fringes, there is a zone of range decrease of ~ -4.5 cm. We can also see a second phase peak (red block close to the maximum) to the southeast with smaller magnitude ($\sim$36 cm). Figure 2b shows a clearer deformation signal in the descending pass covering the whole deformation field. The maximum LOS lengthening and shortening reach $\sim$46.7 cm and ~ -11.8 cm respectively. The similar LOS motion in both passes indicates mainly vertical motion (uplift or subsidence) of the surface. The southeast portion of the deformation field with LOS shortening motion corresponds to the foot-wall side of the west-dipping normal faulting rupture. It has smaller range change values, but covers a larger area compared to the hanging-wall side. The hanging-wall side has densely spaced fringes with two obvious deformation peaks at the center, which can be seen in the ascending pass data as well. The peak away from the mainshock fault has a larger value than the one close to the fault. A close-to-zero surface displacement line can be traced between the hanging-wall side and the foot-wall side. We can see some phase discontinuity at the deformation peak close to the fault because of temporal decorrelation effects [*Zebker and Villasenor*, 1992]. This decorrelation may be due to ground change of ice or frozen earth in this season or due to earthquake related ground disturbance. The two-peak phase feature and the phase gradients suggest that two rupture surfaces contributed to the LOS deformation, but we have no field evidence for this inference, which we explore further in the modeling section, below.

[7] The along-track interferometry result resolves significant horizontal displacements in the area of maximum LOS change (Figure 2c). We can see significant positive (193.4° directed) along-track displacement on the hanging-wall side (the blue area in Figure 2c). There is also an area of smaller 13.4°-directed displacements to the south, but its signal-to-noise ratio is lower than that in the positive area.

Table 1. Envisat ASAR IS2 Mode Data for the Nima Earthquake

	Track	Frame	Preseismic	Postseismic	Baseline
Ascending	341	639$\sim$657	09-08-2007	31-01-2008	136 meter
Descending	348	2943$\sim$2661	23-11-2007	01-02-2008	25 meter

3. Source Models: Fault Geometry and Slip-Distribution Inversion

[8] We use the Okada elastic dislocation algorithm [*Okada*, 1992] to model the coseismic deformation starting with the USGS double couple solutions of the 9 January mainshock and its largest aftershock that occurred a week later. The moment centroid locations of the CMT catalog are offset from the area of surface deformation by about 22 km, suggesting significant errors in the seismic locations. We find that two west-dipping faults with the respective geometry of the CMT nodal planes can be used to match both the along-track motions and the LOS displacements. Single fault model inversion gives a large root-mean-square (RMS) misfit of 4.1 cm and the statistical significance of F-test for the introducing of the second fault reaches 99% (Figure S2 and Table 2). So the two-fault parameterization is essential for the deformation simulation, and the observed

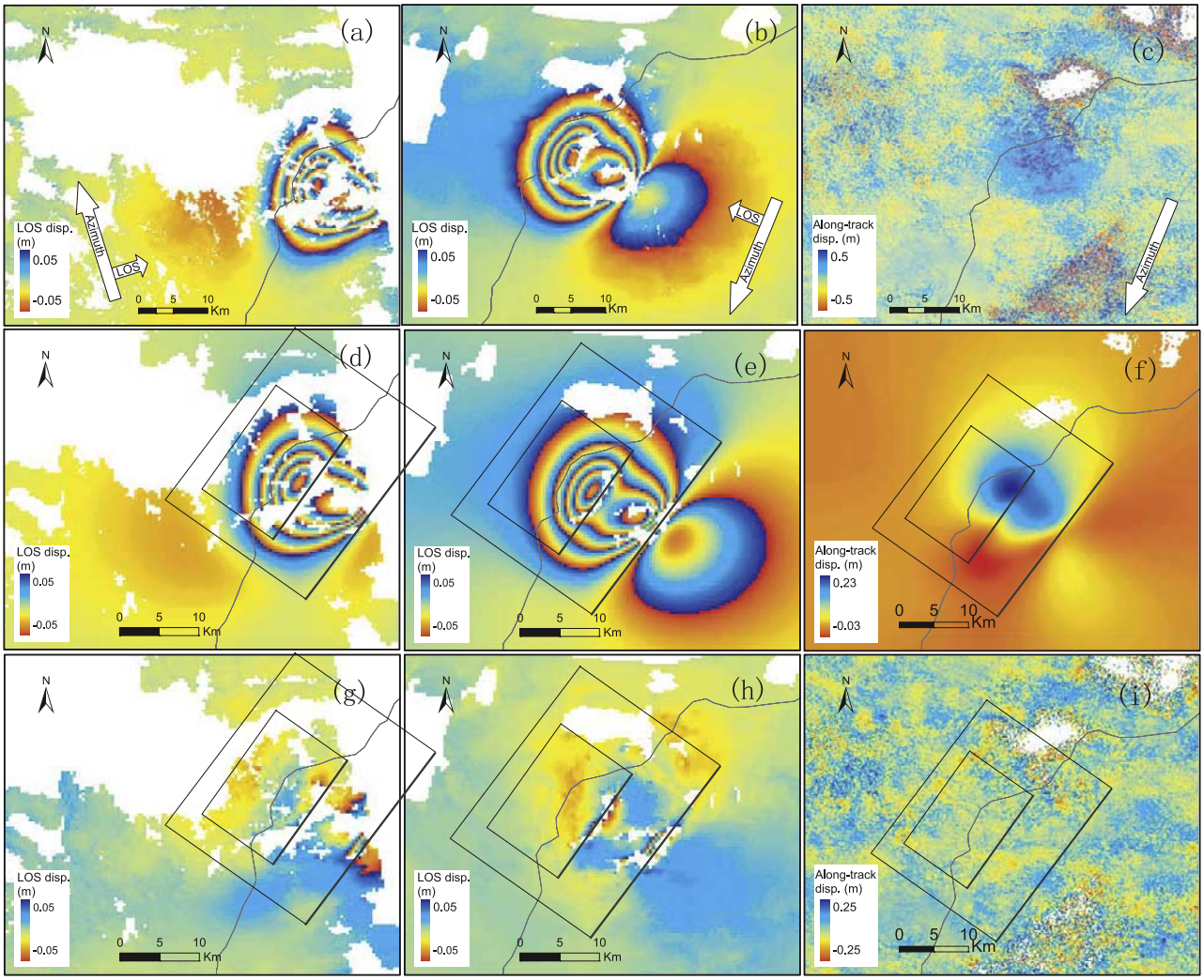

Figure 2. Conventional and along-track interferograms and corresponding deformation simulations of the Nima earthquake. (a) Ascending-pass interferogram. (b) Descending-pass interferogram. (c) Along-track interferogram. (d–f) Interferogram simulation of Figures 2a, 2b, and 2c, respectively, using the slip-distribution solution. (g–i) Phase residuals of the interferogram simulation of Figures 2d, 2e, and 2f, respectively. The grey line and the two black rectangles are the same as in Figure 1. The LOS interferogram is re-wrapping into 10 cm cycles. Note the along-track interferograms have different scale bar.

Table 2. Fault Model Parameters of the Nima Earthquake by Inverting LOS InSAR Data Only Compared With Focal Mechanisms

Fault Number	Length (km)	Width (km)	Depth (km)	Dip (°)	Strike (°)	Latitude (°)	Longitude (°)	Strike-Slip (m)	Dip-Slip (m)	Moment (10^{18} Nm)
1	5.9 ± 0.76	13.0 ± 2.5	2.02 ± 0.26[a]	60.0 ± 1.87	217.3 ± 1.37	32.420 ± 0.0009[b]	85.3504 ± 0.0004[b]	−0.07 ± 0.13	−1.1 ± 0.35	2.57
2	9.3 ± 0.24	3.8 ± 0.57	4.42 ± 0.26[a]	40.03 ± 1.3[c]	194.24 ± 2.4[d]	32.448 ± 0.0023[b]	85.2842 ± 0.0017[b]	−0.41 ± 0.20	−1.8 ± 0.29	1.97
1[e]	-	-	13.3	46.0	206.0	32.300	85.320	-	-	5.02
2[e]	-	-	12.0	46.0	198.0	32.350	85.290	-	-	0.87
1[f]	-	-	19.0	58.0	213.0	32.235	85.180	-	-	5.80
2[f]	-	-	10.0	46.0	196.0	32.319	85.200	-	-	0.72
1[g]	5.45	10.2	5.0	44.0	205.0	32.434	85.316	−0.5	−2.74	4.65

[a]Top depth of the faults.
[b]The middle point location of the fault top.
[c]The fault dip is adjusted to be 50° in the slip-distribution inversion.
[d]The fault strike is adjusted to be 215° in the slip-distribution inversion.
[e]Global CMT solution (www.globalcmt.org/CMTsearch.html).
[f]USGS CMT solution.
[g]Single fault model inversion result.

deformation field does not simply reflect a heterogeneous slip-distribution on the mainshock rupture.

[9] To further improve our knowledge of the kinematics of the composite rupture event involving the M 6.4 mainshock and M 5.9 aftershock, we use formal inversion methods to determine both optimal geometry parameters of two uniform-slip dislocation sources and smoothed distributed-slip models. Prior to inversion, we resampled the continuous deformation field with a quad-tree algorithm [*Jónsson et al.*, 2002] and then fit our model predictions to the 1078 points of LOS displacements and 222 along-track data points. In order to assess the standard deviation of the parameter inversion and the trade-off between any pair of parameters, we produced a large number of observation data sets by propagating the full covariance matrix into the resampled LOS data points, and then the data sets are inverted with the correlated noise. Further detail on the construction of the full covariance matrix can be found in the auxiliary material.

[10] Following the initial estimation of the fault model, we use a global optimization method to search for the best-fitting geometry parameters avoiding convergence at a local minimum misfit. To simplify the inversion procedure, we first invert for fault geometry with uniform-slip assumption. We use the Neighborhood Algorithm (NA) [*Sambridge*, 1999] method to invert for the Nima earthquake parameters with 100 perturbed data sets to assess the statistical properties of the inversion. We use only LOS InSAR data for this purpose because the along-track data has relatively low signal-to-noise ratio, which affects the convergence of the non-linear inversion procedure. Exploration of models that consider the along-track data shows that the misfit is 2–3 times larger than in LOS data inversion and larger phase residuals are produced in the non-linear inversion process. The inverted model fault parameters can be found in Table 2.

[11] The RMS misfit of the final model is 1.74 cm compared to 3.1 cm for our starting model based on the CMT fault geometry (Table 2). Both of the inverted faults dip to the west and do not reach the surface. This confirms the lack of surface rupture found from inspection of the InSAR coherence maps. The estimated seismic moment of the second rupture plane (1.97e + 18 Nm) is larger than the USGS solution for the largest aftershock (0.87e + 18 Nm). This may originate from the uniform-slip assumption or the trade-off between parameters because the slip on the aftershock fault plane is much larger than the slip on the mainshock fault. The along-track prediction (Figure S2c) shows larger negative deformation (12.8 cm) in the south than our along-track observation (less than 5 cm on average) because of the large strike-slip component inverted on the second fault. Most of the residuals in the near field are less than 5 cm except some pixels near the decorrelated area with high phase gradients are larger than 10 cm (Figures S2d and S2e). We find significant phase residual near the aftershock fault. This could be due to seasonal land subsidence, tropospheric artifacts, or the systematic shift of the fault geometry in the uniform-slip inversion, but the misfit can't be further reduced in this inversion.

[12] Once the fault geometry has been determined, the slip-distribution inversion is a linear process with different constraints applied. We fix the fault geometry and invert for the slip distribution on the two fault planes by extending the mainshock fault plane to be 25-km-long and 20-km-wide, and the aftershock fault plane to be 15-km-long and 10-km-wide. We also use the large number of perturbed data sets and estimate the solution uncertainty given the spatially-correlated noise. We use the Fast Non-negative Least Square (FNNLS) inversion method [*Bro and Jong*, 1997] with a 2D Laplace operator for slip smoothing to avoid physically unreasonable solutions. We also constrain the faults to be normal with left-lateral strike-slip components. For the LOS data, we have different perturbed data sets, but for the along-track data, the data is assumed to be spatially uncorrelated with 3 cm standard deviation. We use all of the 1300 points to invert for the slip distribution and compare the results with the inversion of the 1078 LOS data points. Before the inversion, we adjust some of the parameters derived from uniform-slip inversion to suppress possible biases. See the auxiliary materials for details. When the 1300 points are used, a smoothing factor of 2.5 is determined from evaluation of the misfit-roughness trade-off curve (Figure S3). The final solution roughness is ~3.25 cm/km and the misfit is 1.73 cm.

[13] The distributed-slip model and its 1-sigma uncertainty based on consideration of the spatially-correlated noise in the LOS data can be found in Figure 3. Figures 3a and 3c show the solution below 1.5-km depth. The mainshock fault slip reaches ~1.7 m at 6.7~8.4 km (vertical depth) and there is no significant slip below 13.6 km. The left-lateral strike-slip on this fault reaches ~0.9 m at the same depth. The slip on the aftershock fault (maximum 0.85 m) is smaller than that on the mainshock fault and the strike-slip component is also small (maximum 0.35 m). The diagonal terms of the resolution matrix show that the significant slip on both faults is discernable in comparison with the slip at the bottom of the faults (Figure S7). The seismic moment of the two model faults is 5.40e + 18 Nm and 1.09e + 18 Nm respectively, which is closer to the solution of USGS (5.02e + 18 Nm and 0.87e + 18 Nm) than the uniform-slip inversion. Figures 3b and 3d show the 1-sigma uncertainties derived from 100 inversions with the perturbed LOS InSAR data sets and the along-track data with 3 cm standard deviation. On the mainshock fault the slip uncertainty mainly concentrates below 9 km and is less than 3.3 cm. The largest errors occur at 1–7 km along strike where the noise in the data is inverted as pure strike-slip. On the aftershock fault the 1-sigma slip uncertainties are widely distributed, but the maximum uncertainty is less than 1.3 cm, mostly below 3.8-km depth.

[14] If only the 1078-point LOS data is used in slip-distribution inversion, the final misfit is 1.4 cm compared with the 1.74 cm in the geometry inversion. It is interesting to note that a consistent slip-distribution from both data sets can be obtained if the geometry parameters are adjusted after the geometry inversion. The inversion of the combination of the along-track data and the LOS data suppresses the shallow strike-slip slip of the mainshock fault to the north where we don't expect such slip behavior in this normal faulting event (see Figures 3a and S4a). Moreover, the 1-sigma slip uncertainties of the joint inversion are smaller at shallow depth than in inversion of the LOS InSAR data only (Figures 3b, 3d, S4b, and S4d). The difference indicates that the along-track data can be used

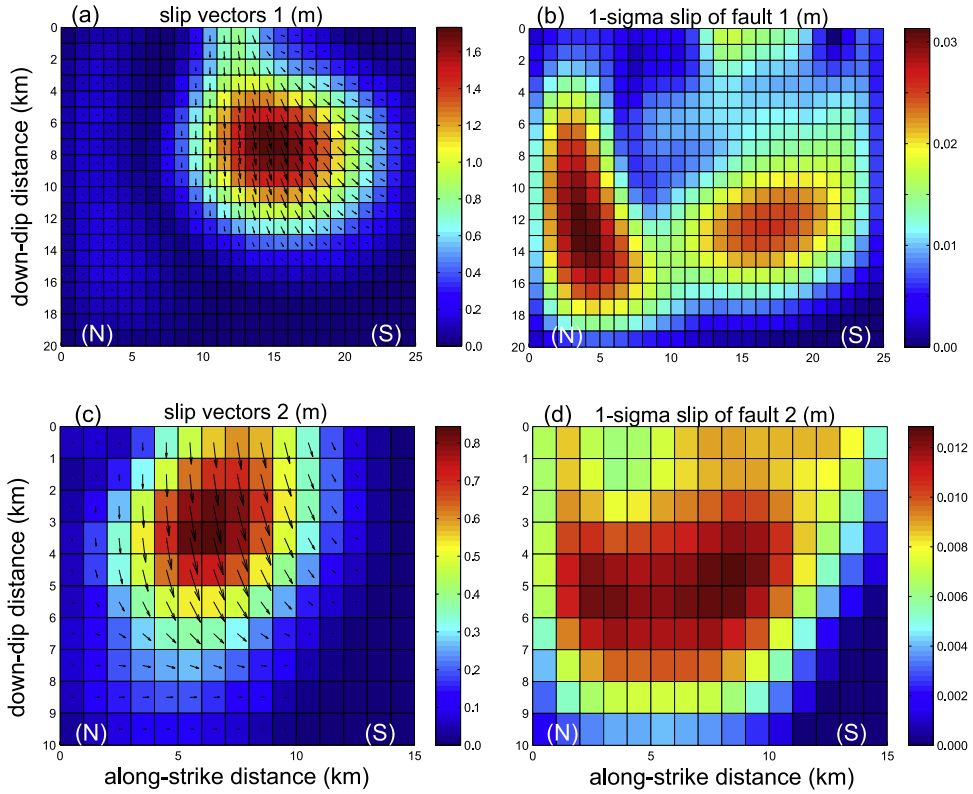

Figure 3. Slip-distribution solutions and their 1-sigma uncertainties. (a and b) Slip-distribution and its 1-sigma uncertainty on the mainshock fault. (c and d) Slip-distribution and its 1-sigma uncertainty on the aftershock fault. The fault planes were divided into 1-km-length by 1-km-width grids. Note that the faults are 1.5-km-depth underground.

to reduce the ambiguity of the LOS InSAR data in the near deformation field and thus improves the resolution of the slip-distributed inversion at shallow depth. We choose the joint inversion result as the final model.

[15] The LOS and along-track deformation prediction and their residuals using the final model are shown in Figure 2. The model fit to all of the 3 observations using the adjusted fault model has been substantially improved compared with the fault geometry inversion. The LOS residuals are concentrated near the faults (Figures 2g and 2h), but their extent is substantially reduced, especially near the aftershock fault. Two patches of residuals in the ascending pass (Figure 2g) reach 5–10 cm at the east edge of the interferogram. We infer that they are due to seasonal land subsidence effects or atmospheric artifacts, because the data time spans autumn and winter. We don't see similar phase patch in the descending pass residuals (Figure 2h). Most of the near-field residuals are lower than 2∼4 cm in both tracks. In particular, the along-track deformation prediction in the north is much larger (<23 cm) than that in the south (<3 cm), which is consistent with our observation.

4. Discussion and Conclusions

[16] We use conventional SAR interferometry and along-track interferometry to extract the ground deformation of the 9 January 2008 Nima earthquake in central Tibet, both in LOS direction of ascending and descending interferograms and in horizontal direction parallel to the descending track. The observation can be simulated with two nearly parallel normal faults dipping to the west. The InSAR-measured deformation includes contributions from the mainshock and its largest aftershock, indicating a composite event of two synthetic normal faults. The seismogenic faults do not reach the surface according to our inversion models and the lack of low-coherence lineaments that would be expected to delineate a surface rupture. Both ruptures are normal faulting with slightly left-lateral strike-slip motion, which is also revealed by the along-track horizontal deformation.

[17] In the analysis of interseismic deformation across this area with a 5.8-year interferogram, *Taylor and Peltzer* [2006] assume pure strike-slip tectonics. In this earthquake we observe normal faulting with a small strike-slip component. In addition to the conjugate fault systems near the Bangong-Nujiang suture zone as revealed by *Taylor et al.* [2003] in their detailed investigation, normal faulting may also significantly contribute to the deformation in this area (around 85.2°E).

[18] **Acknowledgments.** We thank European Space Agency for providing us the ASAR data for this study under Dragon Project 2577. Rita Malosti at ESA kindly helped us plan the radar data acquisitions. We are grateful to S. Barbot for sharing his Along-track Interferometry implementation and helpful discussion. The comments and suggestions of G. Funning and Paul Lundgren greatly helped us improve this manuscript. This work was supported by Basic Research Funding of China Earthquake Adminstration and by State Key Laboratory of Earthquake Dynamics under grant LED2008A08.

References

Barbot, S., Y. Hamiel, and Y. Fialko (2008), Space geodetic investigation of the coseismic and postseismic deformation due to the 2003 M_w7.2 Altai earthquake: Implications for the local lithospheric rheology, *J. Geophys. Res.*, *113*, B03403, doi:10.1029/2007JB005063.

Bro, R., and S. D. Jong (1997), A fast non-negativity-constrained least squares algorithm, *J. Chemom.*, *11*, 392–401.

Deng, Q., P. Zhang, Y. Ran, X. Yang, W. Ming, and Q. Chu (2002), Primary characteristics of China active tectonics (in Chinese), *Sci. China, Ser. D*, *32*(12), 1021–1030.

England, P., and P. Molnar (2005), Late Quaternary to decadal velocity fields in Asia, *J. Geophys. Res.*, *110*, B12401, doi:10.1029/2004JB003541.

Jónsson, S., H. Zebker, P. Segall, and F. Amelung (2002), Fault slip distribution of the 1999 M_w 7.1 Hector Mine, California, earthquake, estimated from satellite radar and GPS measurements, *Bull. Seismol. Soc. Am.*, *92*, 1377–1389.

Molnar, P., and H. Lyon-Caen (1989), Fault plane solutions of earthquakes and active tectonics of the Tibetan Plateau and its margins, *Geophys. J. Int.*, *99*, 123–153.

Okada, Y. (1992), Internal deformation due to shear and tensile faults in a half-space, *Bull. Seismol. Soc. Am*, *82*, 1018–1040.

Peltzer, G., and P. Tapponnier (1988), Formation and evolution of strike-slip faults, rifts, and basins during the India-Asia collision: An experimental approach, *J. Geophys. Res.*, *93*, 15,085–15,117.

Sambridge, M. (1999), Geophysical inversion with a neighbourhood algorithm—I. Searching a parameter space, *Geophys. J. Int.*, *138*, 479–494.

Taylor, M., and G. Peltzer (2006), Current slip rates on conjugate strike-slip faults in central Tibet using synthetic aperture radar interferometry, *J. Geophys. Res.*, *111*, B12402, doi:10.1029/2005JB004014.

Taylor, M., A. Yin, F. J. Ryerson, P. Kapp, and L. Ding (2003), Conjugate strike-slip faulting along the Bangong-Nujiang suture zone accommodates coeval east–west extension and north–south shortening in the interior of the Tibetan Plateau, *Tectonics*, *22*(4), 1044, doi:10.1029/2002TC001361.

Zebker, H. A., and J. Villasenor (1992), Decorrelation in interferometric radar echoes, *IEEE Trans. Geosci. Remote Sens.*, *30*, 950–959.

Zhang, P. Z., et al. (2004), Continuous deformation of the Tibetan Plateau from Global Positioning System data, *Geology*, *32*, 809–812.

R. Bürgmann, Berkeley Seismological Laboratory, University of California, 215 McCone Hall, Berkeley, CA 94720, USA.

Z. Shen, J. Sun, and X. Xu, State Key Laboratory of Earthquake Dynamics, Institute of Geology, China Earthquake Administration, Beijing, China 100029. (sunjianbao@gmail.com)